Distributed feather-inspired flow control mitigates stall and expands flight envelope

Girguis Sedky[a] (ID), Nathaniel Simon[a] (ID), Ahmed K. Othman[a] (ID), Hannah Wiswell[a] (ID), and Aimy Wissa[a,1] (ID)

Multiple rows of feathers, known as the covert feathers, contour the upper and lower surfaces of bird wings. These feathers have been observed to deploy passively during high angle of attack maneuvers and are suggested to play an aerodynamic role. However, there have been limited attempts to capture their underlying flow physics or assess the function of multiple covert rows. Here, we first identify two flow control mechanisms associated with a single covert-inspired flap and their location sensitivity: a pressure dam mechanism and a previously unidentified shear layer interaction mechanism. We then investigate the additivity of these mechanisms by deploying multiple rows of flaps. We find that aerodynamic benefits conferred by the shear layer interaction are additive, whereas benefits conferred by the pressure dam effect are not. Nevertheless, both mechanisms can be exploited simultaneously to maximize aerodynamic benefits and mitigate stall. In addition to wind tunnel experiments, we implement multiple rows of covert-inspired flaps on a bird-scale remote-controlled aircraft. Flight tests reveal passive deployment trends similar to those observed in bird flight and comparable aerodynamic benefits to wind tunnel experiments. These results indicate that we can enhance aircraft controllability using covert-inspired flaps and form insights into the aerodynamic role of covert feathers in avian flight.

bird flight | flow control | bioinspired design | covert feathers | aerodynamics

Birds have inspired aerial vehicle design for centuries due to their ability to fly in various environmental conditions and perform a wide array of flight maneuvers. This ability is partially attributed to the kinematics and dynamics of their primary flight apparatus: the wings. Bird wings are multifunctional systems with structural elements ranging from bones to feathers, each contributing to the functional morphology of flight (1). Wing feathers, for example, are effective flow control devices that mitigate stall and control flow separation (2). One such feather system is known as the covert feathers (or coverts).

Covert feathers (Fig. 1*A*) are contour feathers; they provide the upper surface contour and most of the lower surface contour over the thick forward sections of the wing (3). Bird wings have multiple rows of covert feathers, and several of these feather rows have been observed to deploy during flight, particularly in response to gusts or during landing (both high angle of attack maneuvers) (4). The aerodynamic function of covert feathers in birds is understudied; only a few studies have observed the behavior of covert feather deployment in flight or during wind tunnel experiments on cadaver wings (4, 5). While these studies suggest covert feathers function as aeroelastic devices, these insights are mostly qualitative, underscoring the need for a comprehensive aerodynamic assessment (6).

In addition to biology studies, numerous engineering studies have designed covert-inspired suction-side flaps to serve as flow control devices in poststall conditions. While these studies have investigated a broad spectrum of flap flexibility (e.g., rigid, flexible, and hairy flaps) and mobility properties (e.g., static, freely moving, and torsionally hinged flaps) (7–11), almost all have only considered a single flap, overlooking the multirow covert feather arrangement found in birds. Only two studies have considered a system of more than one covert-inspired flap. In the first study, Nair et al. (12) numerically studied the performance characteristics of a covert-inspired passive flow control technique involving a system of five torsionally hinged flaps mounted on the upper surface of a poststall airfoil at a low Reynolds number ($Re = 1,000$). The results of their study show a maximum lift improvement of 25% at an angle of attack $\alpha = 20°$ for the single flap case and that adding more flaps reduces overall lift improvements. The second is an experimental study by Bramesfeld and Maughmer (13) where they evaluated two movable tabs on the suction side near the trailing edge of an S824 airfoil at $Re = 10^6$. The results show that the additional tab does not significantly improve lift compared to

Significance

Multiple rows of covert feathers contour bird wings, and studies suggest they can enhance flight during maneuvers such as landing or flying through gusts. However, there is no existing consensus on their underlying physics or the implications of having multiple rows. Using a system of covert-inspired flaps, we identify two distinct location-sensitive aerodynamic mechanisms and determine their additivity. We find that a covert-inspired flap system exploiting both mechanisms improves aerodynamic efficiency and stability. Implementing these flaps on a bird-scale airplane reveals that a passive, stall-initiated deployment of the flaps, similar to that observed in bird flight, expands the flight envelope. Results from this study can improve aerial vehicle design and provide insight into the covert feathers' role in bird flight.

Author affiliations: [a]Department of Mechanical and Aerospace Engineering, Princeton University, Princeton, NJ 08544
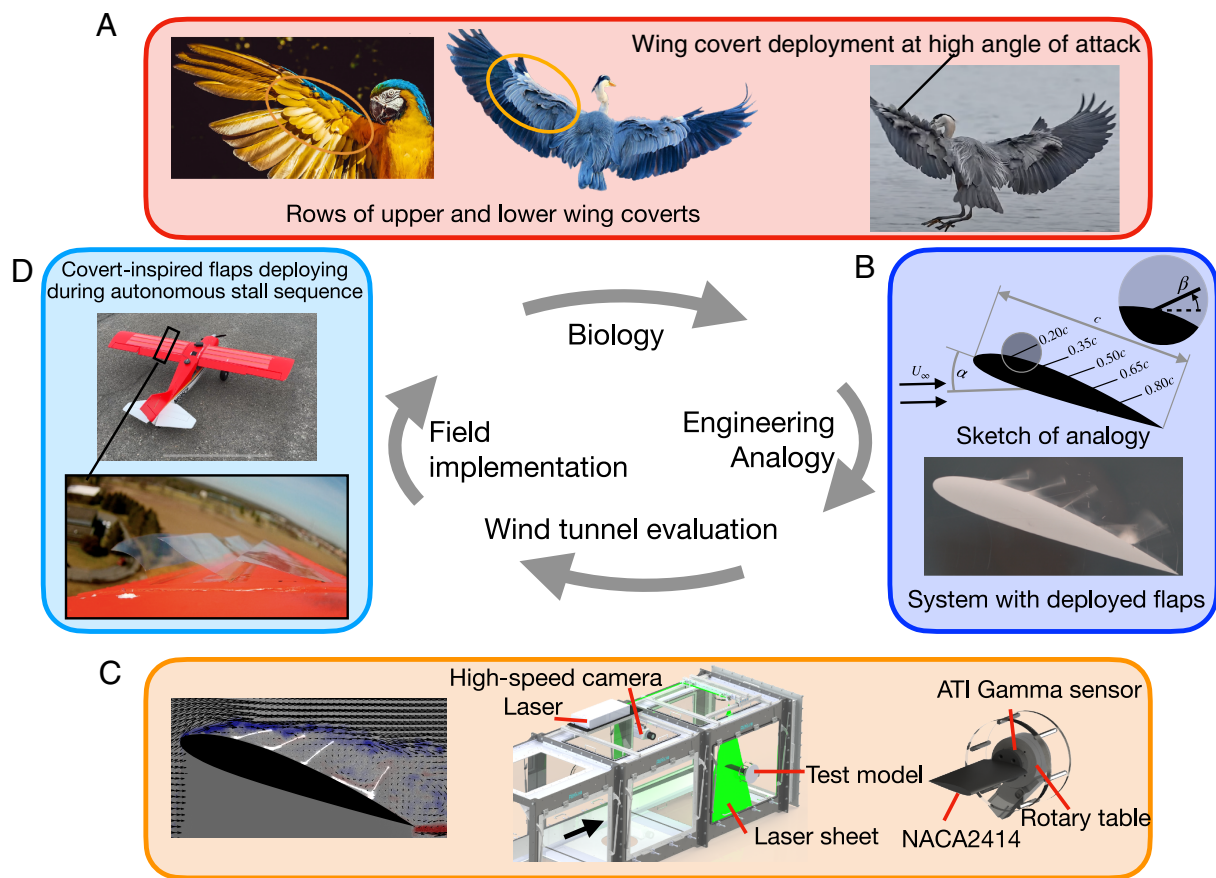
Fig. 1. The bioinspired design process associated with designing and evaluating the distributed and passive covert-inspired flow control system showing: (*A*) *The inspiration* of multiple rows of covert feathers on the *Bottom* surface of a parrot wing (*Left*) and *Upper* surface of a heron wing (*Middle*). *Upper*-surface covert feathers deploying during a high angle of attack maneuver (*Right*) (Photo Credit: Pixabay), (*B*) *The engineering analogy* consisting of five covert-inspired flaps distributed on the suction side of an airfoil (Movie S1), (*C*) *The evaluation approach* using wind tunnel experiments (*Middle*) to identify and isolate the key physical principles and flow control mechanisms of covert-inspired flaps using flow field measurements (*Left*) and integrated force-torque measurements (*Right*), and (*D*) *Field implementation* by adding the spatially distributed covert-inspired flow control device on a remote controlled bird-scale airplane and performing power-on stall maneuvers during flight.

the single tab. The results from both of these studies may imply the lack of aerodynamic utility of the multirow arrangement observed in covert feather systems. However, the limited observed benefits can be attributed to the Reynolds number dependence, in the case of ref. 12, and the trailing edge placement of the movable tabs, in the case of ref. 13.

Presently, we have a limited understanding of the flow physics underlying the aerodynamic benefits of covert feathers and the impact of multirow covert feather systems at Reynolds numbers relevant to bird flight ($Re \approx 10^5$). To bridge this gap, this paper conducts an experimental exploration and evaluation of a biologically relevant covert feather analogy at such Reynolds numbers. Our simplified analogy of the covert feather system consists of five spatially distributed and passively deployable flaps along the suction side of an airfoil (Fig. 1*B*). Through detailed experimental analyses encompassing time-resolved and averaged flow fields, integrated force measurements, and flight testing (Fig. 1 *C* and *D*), we seek to answer the following questions:

Q1: What are the flow physics and resulting aerodynamic forces of a single covert-inspired flap in poststall flight regimes, and how do such physics vary as a function of the flap's location?

Q2: What is the additivity of the flow control mechanisms uncovered in Q1 for a multirow covert-inspired flap system?

Q3: How do the findings from wind tunnel experiments translate to the in-flight performance of an aerial vehicle?

Addressing these questions establishes a foundational understanding of the flow physics of the covert-inspired flap system which can be used to expand the flight envelope of uncrewed aerial vehicles (UAV) and form hypotheses about the role of these feathers during bird flight (Fig. 1).

1. Results and Discussion

1.1. Wind Tunnel Experimental Evaluation. In this section, we present the results of our wind tunnel experiments, which include force and particle image velocimetry (PIV) measurements. These measurements reveal and quantify the flow physics that govern the airfoil-flap system. We first focus on a single flap on the suction side of the airfoil at various chordwise locations to answer our first research question. We then examine the multirow flap system to answer our second research question. This structured approach allows us to systematically explore the flow control mechanisms of covert-inspired flaps at a relevant Reynolds number.

Single-flap deployment and the flow physics underlying covert-inspired flow control. Bird wings have covert feather rows at various chordwise locations. Because aerodynamic flow conditions vary

along a wing's chord, the way in which various covert feather rows interact with the flow may also differ substantially. Here, we perform wind tunnel assessments of an engineering analogy consisting of an airfoil with a single flap mounted at one out of five possible locations along the airfoil's suction side (Fig. 2). In this analysis, we use a binary naming convention where "1" indicates the presence of a flap and "0" indicates the absence of a flap at the corresponding location (e.g., "10000" refers to a configuration where the flap is mounted close to the leading edge). Because covert feathers are stall-mitigating devices, this section focuses on the poststall behavior of the flap-airfoil system at $\alpha > 16°$. The reduction in lift at prestall angles of attack ($\alpha < 16°$, Fig. 2A) can be attributed to early flap deployment, which disrupts the otherwise attached flow on the airfoil's suction side. In the poststall regime, all single-flap cases exhibit higher lift coefficients, and most single-flap cases (with the exception of the trailing-edge flap case "00001") exhibit lower drag coefficients relative to the baseline with +95% confidence (Fig. 2 A and B). This indicates that a passively deployed flap placed at any of the five locations along the wing's suction side is an effective flow control device. To understand the mechanisms responsible for poststall

lift improvement and drag reduction of the single-flap cases, we focus on $\alpha = 20°$, where most single-flap cases have similar lift improvements. For each of these configurations, we analyze the time-averaged flow fields (*Top* row of Fig. 2C), the time-averaged pressure fields (*Bottom* row of Fig. 2C), and the edge of the separated shear layer (Fig. 2D). Even though the enhancement in lift is comparable for all single-flap cases, flow field measurements shown in the first row of Fig. 2C show distinct flow patterns for the leading-edge flap "10000" and the trailing-edge flap "00001" cases, suggesting that even for similar lift enhancements, the flow physics are different.

The *Top* row of Fig. 2C shows that the leading-edge flap interacts with the separated shear layer. Comparing the shear layer edge location of the baseline with the leading-edge flap case in Fig. 2D, it is observed that the interaction of the leading-edge flap with the shear layer brings it closer to the airfoil's surface. This interaction is manifested in the time-averaged pressure fields in the *Bottom* row of Fig. 2C, which reveal that the leading-edge flap case exhibits a low-pressure zone ahead of the flap. This low-pressure zone is reminiscent of the high suction peak at the leading edge observed for airfoils with attached flows. Synthesizing the
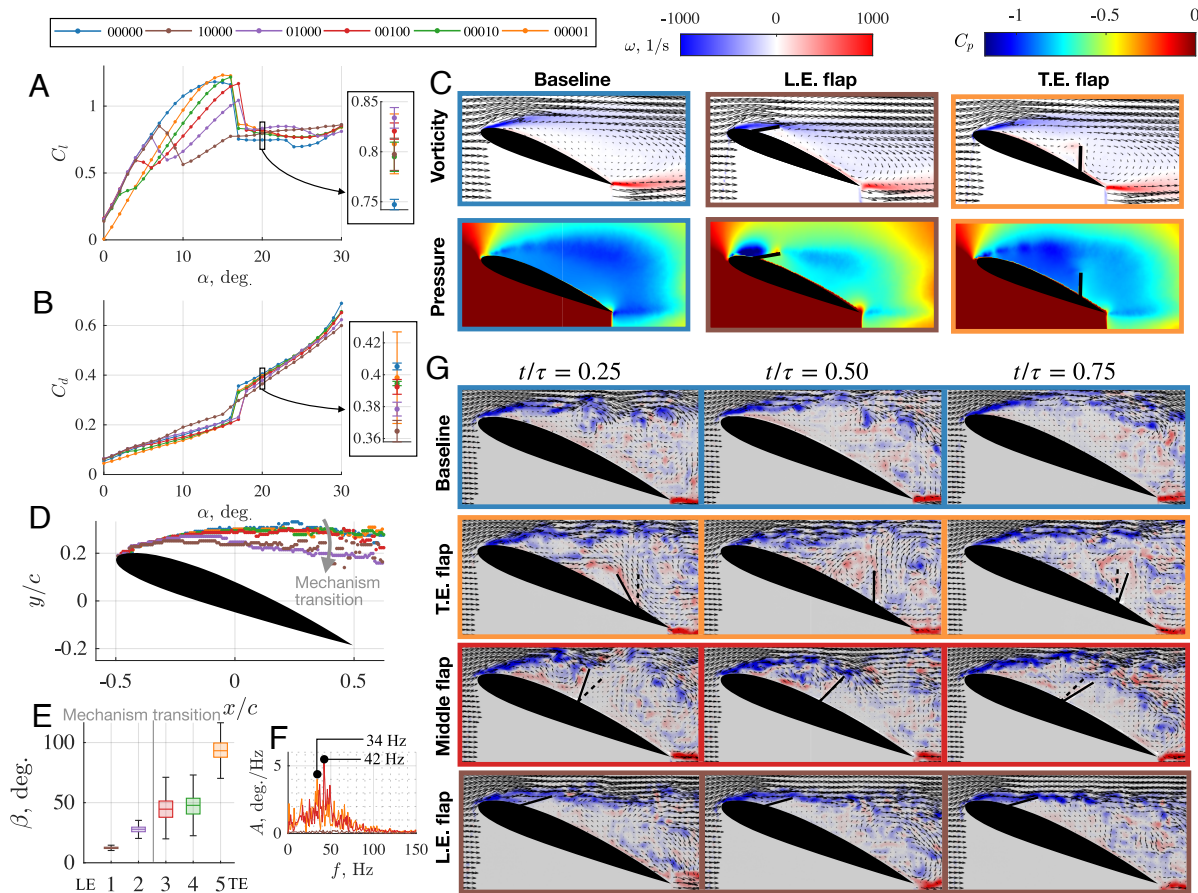

Fig. 2. Aerodynamic force and flow field measurements of single covert-inspired flaps at various locations along the airfoil's surface showcasing the various position-dependent flow control mechanisms. (A) Coefficient of lift C_l and (B) drag C_d as a function of angle of attack α highlighting the mean values and 95% CIs at $\alpha = 20°$. (C) Time-averaged vorticity ω and velocity fields in the *Top* row, and time-averaged coefficient of pressure measurements relative to the free stream C_p in the *Bottom* row for angle of attack $\alpha = 20°$. Baseline case 00000 on the *Left*, trailing-edge (T.E.) flap case 00001 in the *Middle*, and leading-edge (L.E.) flap case 10000 on the *Right*. (D) Separated shear layer edge location for all single-flap cases at angle of attack $\alpha = 20°$ showing the transition in the flow control mechanism between 00100 and 01000. (E) Box plot showing the median and spread of the flap deflection angles β demonstrating how different flow control mechanisms are associated with different flap deflection amplitudes. (F) Energy spectrum of the flap deflection angles for the trailing-edge flap case 00001 (orange), *Middle*-flap case 00100 (red), and leading-edge flap case 10000 (brown). (G) Instantaneous vorticity ω and velocity field measurements at angle of attack $\alpha = 20°$ for the baseline 00000 (first row), trailing-edge flap case 00001 (second row), *Middle*-flap case 00100 (third row), and leading-edge flap case 10000 (*Bottom* row) at different points in time. The dashed line represents the mean flap position while the solid line represents the instantaneous flap position.

shear layer edge location, the flow fields, and pressure fields reveals that in poststall conditions, the deployment of the leading-edge flap alters the effective airfoil surface geometry. This leads to a reduction in the adverse pressure gradient the flow encounters. The reduction in the adverse pressure gradient reduces the degree of flow separation, which recovers the suction peak at the airfoil's leading edge, improving lift. This aerodynamic enhancing mechanism is referred to as the shear layer interaction mechanism for the remainder of the paper.

Unlike the leading-edge flap, the separated shear layer of the baseline and the trailing-edge flap cases coincide (Fig. 2D), suggesting that the trailing-edge flap improves poststall aerodynamic performance via a mechanism different from that of the leading-edge flap. Even though the trailing-edge flap case exhibits a flow with similar flow separation to the baseline, the flow field on the suction side of the airfoil shown in the *Top* row of Fig. 2C is significantly different. For the trailing-edge flap case, two recirculation zones can be observed upstream and downstream of the flap. The trailing-edge flap is observed to block the reversed flow downstream of it, creating the downstream recirculating zone. At the same time, the leading edge shear layer rolls upstream of the flap, creating the second, upstream recirculating zone. The corresponding time-averaged pressure field (Fig. 2C, *Bottom* row) shows that the trailing-edge flap creates a barrier between two distinct pressure zones, indicating that the trailing-edge flap improves lift through the pressure dam effect that observed in previous studies (12–14). The deployed flaps act as a barrier or a splitter plate, preventing the relatively high pressure downstream from propagating upstream of the airfoil, allowing a lower pressure region to be maintained upstream of the flap, improving lift. The trailing-edge flap's flow control mechanism is referred to as the pressure dam effect for the remainder of this paper. The drag reduction in the leading-edge flap case can be explained by examining the pressure fields. In the leading-edge flap case, the pressure is redistributed along the airfoil's surface such that the high suction regions are concentrated toward the airfoil's leading edge where the surface normal vector orientation has a lower horizontal component, reducing the drag contribution. In addition to showing the difference in the shear layer location between the leading- and trailing-edge flap cases, Fig. 2D highlights the location-dependent transition between the two mechanisms. Specifically, while cases "01000" and "10000" bring the shear layer closer to the airfoil, engaging the shear layer interaction mechanism, cases "00001," "00010," and "00100" primarily engage the pressure dam effect without affecting the shear layer location.

The location-sensitive flow control mechanisms are not only manifested in the flow field, but they are also evident in the behavior and dynamics of the flaps themselves. Fig. 2E shows that single-flap cases that engage the pressure dam mechanism (e.g., "00001," "00010," and "00100") exhibit large fluctuations in their flap deflection angle β (as defined in Fig. 1B) while cases that engage the shear layer interaction mechanism (e.g., "01000" and "10000") have very low flap angle fluctuations. *SI Appendix,* Appendix A1 includes additional information regarding the deflection angle fluctuations of each flap. The deflection angle spectrum presented in Fig. 2F showcases that the flap dynamics are not periodic, containing a variety of frequencies. At this Reynolds number, the flow contains many time and length scales, which provide a broad-spectrum forcing to the flap, leading to aperiodic and broad-spectrum flap dynamics. Nevertheless, the energy spectrum for the leading-edge flap case is significantly lower due to the low amplitude fluctuations that the flap

experiences. Even though the dynamics of the flap contain a broad frequency spectrum, we identify a period τ based on the frequency of the highest peak of the deflection angle spectrum in Fig. 2F. The period τ is determined for flaps with significant oscillations, namely, the trailing-edge flap and the *Middle* flap cases only. Since the baseline and leading-edge flap cases do not have a signature peak flap frequency, we present their instantaneous snapshots based on the peak frequency of the trailing-edge flap case. Based on this period, we identify a representative flap cycle and present instantaneous snapshots of the flow field at various times t/τ of that cycle in Fig. 2G. (Full instantaneous flow measurements can be seen in Movies S2–S5). The instantaneous flow fields show that the trailing-edge flap mainly interacts with the separated wake, experiencing large fluctuations due to the vortex roll-up upstream as well as the reverse flow downstream. The *Middle* flap is in an intermediate location where it interacts mainly with the wake but also with the leading-edge shear layer. The flap dynamics are thus influenced by the strong vortex roll-up upstream. Finally, the leading-edge flap acts to reduce flow separation by interacting with the steady shear layer, and thus, it experiences low fluctuations, and its deflection angle remains relatively constant when compared to the *Middle* and trailing-edge flaps.

Multiple-flap deployment and the additivity of the flow control mechanisms. In this section, we explore the aerodynamic role of the multiple rows of covert feathers and investigate whether the location-dependent flow control mechanisms are sensitive to the number of additional covert rows. We present results for two sets of configurations, referred to as leading-edge and trailing-edge deployment. In the leading-edge deployment set, we investigate configurations in which the flaps are deployed successively from the leading edge to the trailing edge of the airfoil, namely, configurations {10000, 11000, 11100, 11110, 11111} (Fig. 3 A–C). In this set, the shear layer interaction flow control mechanism is activated first. In the trailing-edge deployment set, we investigate configurations in which the flaps deploy from the trailing edge to the leading edge of the airfoil, namely, configurations {00001, 00011, 00111, 01111, 11111}. In this set, the pressure dam flow control mechanism is activated first (Fig. 3 D–F).

The time-averaged flow fields for the leading-edge flap deployment, shown in the *Left* column of Fig. 3A, and the corresponding shear layer location, presented in Fig. 3B, demonstrate that successive deployment of the first three flaps results in a successive decrease in the height of the shear layer. This, in turn, corresponds to a successive increase in the suction peak at the airfoil's leading edge (*Right* column of Fig. 3A). These observations reveal that the shear layer interaction mechanism has an additive nature. Each additional flap deployed interacts with the shear layer emanating from the upstream flap, increasing the overall deflection of the shear layer and enhancing the suction peak experienced by the airfoil at its leading edge. In contrast to the deployment of the first three flaps, deploying a fourth flap considerably changes the flap system response and the flow field. When the fourth flap is deployed (last row in Fig. 3A), the third flap closes. This indicates that the deployment of the fourth flaps engages the pressure dam mechanism, effectively shielding the third flap from the high-pressure zone in the wing's wake that would normally elevate it. Also, considering the third flap's distance from the upstream low-pressure region, which might otherwise induce an upward force, the third flap does not encounter sufficient force to overcome its own weight and deploy. The additive nature of the shear layer interaction mechanism observed in the flow measurements is reflected in the mean coefficients of lift C_l and
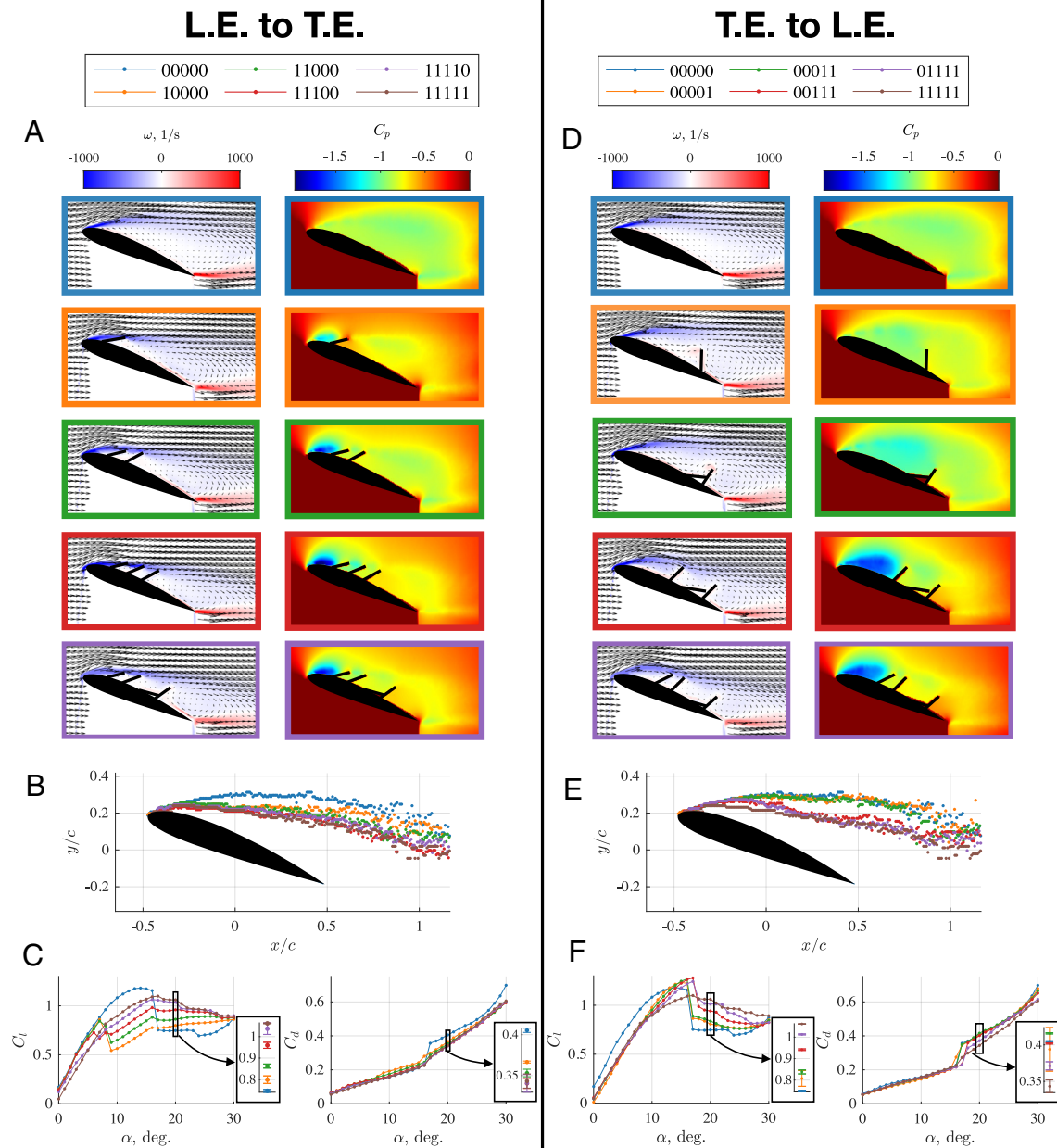
Fig. 3. The flow physics and aerodynamic performance associated with the multi-row covert-inspired airfoil-flap system at $\alpha = 20°$. The *Left* column presents cases with successive flap additions starting from the leading edge (denoted: L.E.), in which the shear layer flow control is activated first. *A* shows the time-averaged vorticity ω (left sub-column) and coefficient of pressure relative to the free stream C_p (right sub-column) along with the airfoil-flap silhouette showing the mean flap position. *B* shows the separated shear layer edge locations. *C* shows The coefficient of lift C_l (left sub-column) and coefficient of drag C_d (right sub-column) as a function of angle of attack, highlighting the mean values and 95% CIs at $\alpha = 20°$. The *Right* column presents cases with successive flap additions starting from the trailing edge (denoted: T.E.), where the pressure dam flow control mechanism is activated first. *D* shows the time-averaged vorticity ω (left sub-column) and coefficient of pressure relative to the free stream C_p (right sub-column) along with the airfoil-flap silhouette showing the mean flap position. E shows the separated shear layer edge locations. *F* shows the coefficient of lift C_l (left sub-column) and coefficient of drag C_d (right sub-column) as a function of angle of attack, highlighting the mean values and 95% CIs at $\alpha = 20°$.

drag C_d of the airfoil (Fig. 3*C*). The lift enhancement in the poststall regime increases with the deployment of each additional flap. The lift enhancement is accompanied by a reduction in drag relative to the baseline as the wake of the airfoil becomes narrower.

In the case of trailing-edge flap deployment, deploying a flap directly ahead of the trailing-edge flap ("00011") creates no appreciable difference in the time-average pressure field (second and third rows of Fig. 3*D*) nor the aerodynamic forces (Fig. 3*F*). In fact, that additional flap remains undeployed for the same

reason the third flap remains undeployed in the "11110" case. The trailing-edge flap improves lift by acting as a pressure dam, separating the upstream low pressure from the downstream high pressure. Once the pressure zones are separated, an additional flap ahead of the trailing-edge flap separating the low-pressure zone further does not lead to additional aerodynamic benefits. Thus, unlike the shear layer interaction mechanism, it is observed that the pressure dam effect does not provide any additional aerodynamic benefit with the addition of extra flaps, making it a non-additive flow control mechanism. In contrast to the "00011"

case, deploying a third flap ("00111") creates an appreciable change to the pressure field (fourth row of Fig. 3D) and results in additional lift gains (Fig. 3F). A suction peak also emerges in the time-averaged pressure field (Fig. 3D), and the shear layer is observed to deflect relative to the baseline in Fig. 3E. This indicates that the shear layer interaction mechanism is now being engaged. As more forward flaps are deployed, the shear layer deflects further down, further enhancing lift and confirming the additive nature of the shear layer flow control mechanism.

By exploiting the additive nature of the shear layer interaction and combining it with the pressure dam effect, the all-flap configuration ("11111") improves lift by up to 45% and reduces drag by up to 31% in the poststall regime (Fig. 4 A and B). Fig. 4 A and B also show a much more gradual stalling behavior relative to the baseline case, as observed by the lack of sudden changes in the lift or drag curves. The average flow fields presented in Fig. 4D showcase a significantly deflected shear layer and a pressure dam created by the trailing-edge flap preventing wake backflow. To investigate the coexistence of the two mechanisms, Fig. 4E presents the shear layer location of the baseline "00000," the all-flap case "11111," and the three-flap case "11100" which only exploits the shear layer interaction mechanism. Both the all-flap case and the three-flap case "11100" deflect the separated shear layer equally. Nevertheless, Fig. 4A shows that the all-flap case produces higher lift for the greater part of poststall regime. This is evidence that the additional performance gain produced by the all-flap case is not due to further amplification of the shear layer interaction mechanism relative to the three-flap case but

is due to engaging the pressure dam flow control mechanism. This result suggests that covert flaps not only enhance lift using different mechanisms but that these physical mechanisms can also be exploited simultaneously. The culmination of these effects produces a pressure distribution that increases the longitudinal stability of the airfoil, as shown in the variation of the pitching moment coefficient C_m about the airfoil's aerodynamic center (quarter chord) in Fig. 4C. The gentler stall behavior of the all-flap case mitigates the abrupt pitching moment transition experienced by the baseline during stall. In addition, the negative C_m slope coupled with the higher extrapolated C_m at $\alpha = 0$ of the all-flap case poststall suggests that flap deployment enhances pitch or longitudinal stability relative to the baseline case.

In addition to the additive aerodynamic benefits of the multiflap system, Fig. 4F showcases the alteration of each flap's dynamics upon the deployment of other flaps. For the rearward four flaps, the fluctuations of the flap dynamics are lower for the all-flap case ("11111") compared to the corresponding single flap cases. For the leading-edge flap, the flap interacts with the separated shear layer in both the single and all-flap cases, and thus, the presence of additional flaps does not affect the flap's mean deflection or fluctuations. For the remaining flaps, the reduction in fluctuations is less substantial for the flaps that engage the shear layer interaction mechanism (e.g., the second flap) than for the flaps that engage the pressure dam effect (e.g., the fifth flap). The fourth flap does not deploy in the all-flap case because the fifth flap engages the pressure dam flow control
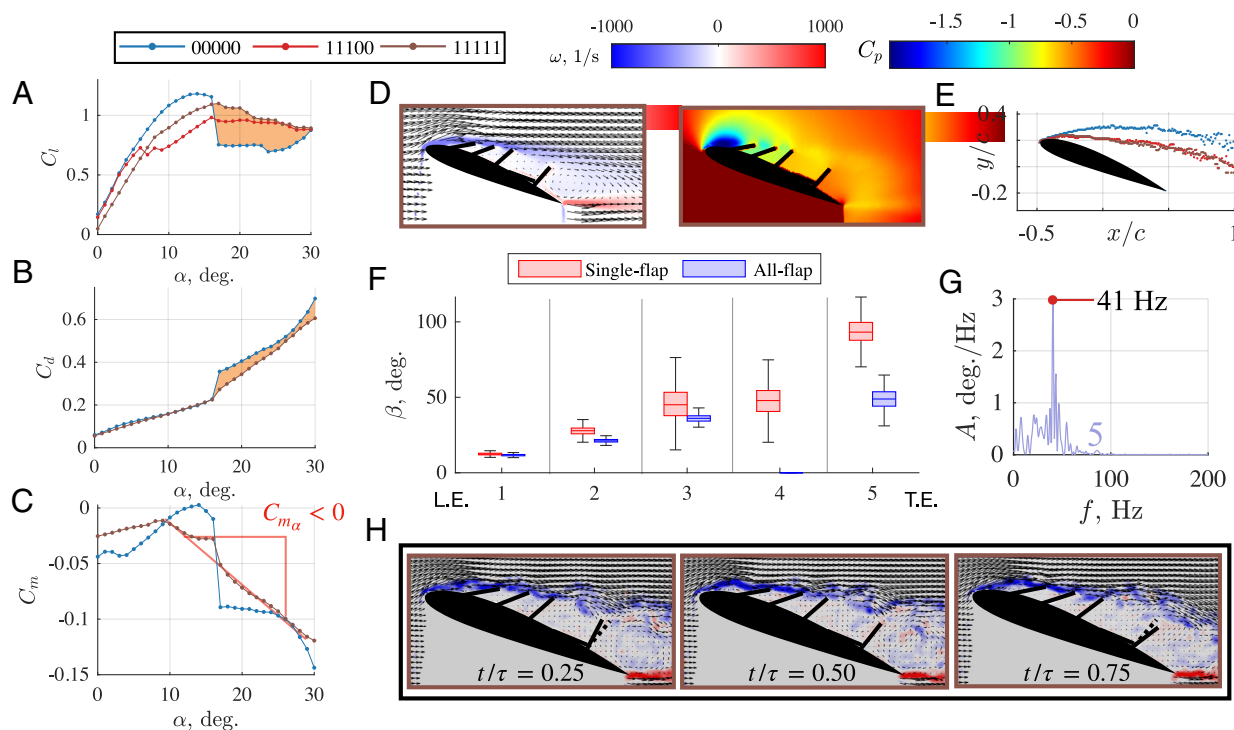

Fig. 4. Aerodynamic load and flow field measurements of the all-flap case showcasing lift enhancement up to 45% and drag reduction of up to 31% in the poststall regime, in addition to the flaps' effects on the pitching moment and the flow field. Flow fields, pressure fields, and flap dynamics are presented for $\alpha = 20°$. (A) Coefficients of lift C_l, (B) drag C_d, and (C) pitching moment about the airfoil's quarter chord C_m as a function of angle of attack α. The orange regions represent the increase in C_l and the decrease in C_d, respectively in the poststall regime. (D) Time-averaged vorticity ω and velocity fields (*Left* column) and time-averaged coefficient of pressure measurements relative to the free stream pressure (*Right* column) at $\alpha = 20°$. (E) Separated shear layer edge location for the baseline 00000, three-flap case 11100, and five-flap case 11111. (F) Box plot showing the median and spread of the flap deflection angles β of every flap in the all-flap case, as well as the corresponding single flap case. (G) Energy spectrum of the deflection angles for the trailing-edge flap in the all-flap case. (H) Instantaneous vorticity ω and velocity field measurements for the all-flap case at different points in time t during a representative cycle with period τ based on the peak amplitude frequency corresponding to the trailing-edge flap energy spectrum in (G).

mechanism and shields the fourth flap. The third flap experiences the most substantial reduction in fluctuations when the other flaps are simultaneously deployed. Deployment of the two flaps upstream of the third flap brings the shear layer closer. In turn, the third flap becomes driven by the shear layer, which reduces its fluctuations, indicating that the flow control mechanism of the third flap switches from the pressure dam effect in the single-flap case to the shear layer interaction mechanism in the all-flap case. This result is also supported by the flow field and force measurements presented in Fig. 3*A*. *SI Appendix*, Appendix A1 includes additional information regarding the deflection angle fluctuations of the all-flap configuration.

To examine the instantaneous flow field, a cycle period $\tau = 41$ Hz is identified based on the frequency of the maximum amplitude, which belongs to the trailing-edge flap (full instantaneous flow measurements can be seen in Movie S6). Based on this period, we identify a representative flap cycle and present instantaneous snapshots of the flow field at various times t/τ of that cycle in Fig. 4*H*. The instantaneous snapshots highlight the stability of the shear layer over the first three flaps, suggesting the effective rearward motion of the separation point. The deflections of the trailing-edge flap are still governed by the airfoil wake dynamics, and thus, its oscillations around the mean deflection angle are noticeable at various points throughout the representative flap cycle. The rearward movement of the separation point, along with the pressure field redistribution, explains the lift enhancement, drag reduction, and augmented longitudinal stability.

1.2. In-Flight Experimental Evaluation. Wind tunnel experiments demonstrate the additive benefits of a multicovert flap system, including lift enhancement, drag reduction, and increased longitudinal stability (Fig. 4). In this section, we demonstrate that these improvements extend to aerial vehicles in flight: mitigating the effects of stall and extending the flight envelope to higher angles of attack at Reynolds numbers of Re = 100,000 to 500,000, well within the range of bird flight ($Re \approx 10^5$). This analysis answers our third research question and closes the bioinspired process loop (Fig. 1), informing hypotheses on the role of covert feather systems in avian flight.

We demonstrate the effectiveness of covert-inspired flaps at mitigating stall and expanding the flight envelope through a power-on stall maneuver. In this maneuver, the aircraft employs a combination of flight control and power inputs to continuously increase the angle of attack while maintaining level flight until a stall occurs. Fig. 5*B* (Movie S7) depicts a characteristic power-on stall sequence: Airspeed decreases while the aircraft pitch angle θ and the angle of attack of the airflow incident to the aircraft α increase simultaneously until the point of stall ($\alpha \approx 40°$). As the wings stall fully, they cannot produce sufficient lift, causing the aircraft to pitch down. The two cases we compare in this analysis are referred to as "Coverts" and "Baseline." The Coverts configuration consists of three distributed covert flaps on the wing's suction side that correspond to the configuration "11100" (Figs. 1*D* and 5*A*), while the Baseline refers to the standard configuration without covert flaps. The "11100" configuration was chosen for flight testing over others due to the significant demonstrated aerodynamic benefits while avoiding interference with the trailing-edge control surfaces of the aircraft (i.e., the flaps and ailerons). Thus, during the flight test, we are mainly exploiting the shear layer interaction flow control mechanism to mitigate stall.

We define stall as a sudden, uncommanded decrease in α. To ensure repeatability of trials and conditions, these stall sequences were performed autonomously by an onboard closed-loop flight controller. Similar to the wind tunnel experiments, Fig. 5 *A* and *B* show that the covert flaps deploy passively once the aircraft reaches a sufficient angle of attack $\alpha \geq 20°$. The flap closest to the trailing-edge deploys the most, reaching nearly 90° at stall. Over the course of 19 power-on stalls ($12\times$ for Coverts and $7\times$ for Baseline), we demonstrate that covert flaps increase the average α_{max} by 9%—from 45° to 50° (Fig. 5 *C* and *D*). This increase in performance effectively delays the stall. Aligning the stalls in time (Fig. 5*C*), we notice that the mean covert stall time $\bar{t}_{stall}^C$ effectively occurs 0.15 s after the mean baseline stall time $\bar{t}_{stall}^B$.

Compared to the Coverts case, the Baseline stall was observed to be more aggressive, often coupled with a significant uncommanded roll to the left. This left-turning tendency is well documented in powered aircraft, particularly at low speeds and high power settings, and can be attributed to propeller torque, P-factor, and gyroscopic precession (15). Fig. 5*D* compares the maximum angle of attack α_{max}, maximum roll angle magnitude $|\phi|_{max}$, and maximum roll angle rate magnitude $|p|_{max}$ for both cases during the stall sequence. The $|\phi|_{max}$ and $|p|_{max}$ quantities demonstrate the particularly aggressive baseline stall behavior characteristic of power-on stalls, which the covert flaps mitigate, decreasing $|\phi|_{max}$ by 24% and $|p|_{max}$ by 39%.

After initiating a stall sequence, the sequence is either terminated after one second or when a loss of control occurs, triggering a recovery sequence. We measure loss of control through the loss of control ratio (LOCR), or the percentage of stall sequences that depart controlled flight and require the recovery maneuver. The Baseline stalls lost control more rapidly and frequently than Covert stalls, as shown in Fig. 5*E*. Specifically, 86% of Baseline stalls lose control within one second of stall, compared to only 33% of Covert stalls within two seconds. This increase in vehicle longitudinal stability is in line with the findings of the wind tunnel experiments (Fig. 4*C*), specifically the negative slope of C_m vs. α for the "11111" covert case.

In summary, our flight testing experiments demonstrate that the aerodynamic improvements of covert flaps observed in the wind tunnel translate to in-flight improvements when covert flaps are integrated into an aerial vehicle. Through an autonomous power-on stall maneuver designed to reach high angles of attack, we show that the covert-inspired flaps deploy passively during the maneuver. The deployment of covert flaps increases the maximum angle of attack, effectively delaying stall while simultaneously increasing the stability of the vehicle—resulting in longer durations of poststall control and fewer departures from controlled flight.

2. Conclusion

This article sets out to answer three questions related to the flow control mechanisms underlying covert-inspired flaps at a Reynolds number relevant to both avian flight and small UAV operations: (Q1) What are the flow physics and resulting aerodynamic forces of a single covert-inspired flap in poststall flight regimes, and how do such physics vary as a function of the flap's location?, (Q2) What is the additivity of the flow control mechanisms uncovered in Q1 for a multirow covert-inspired flap system?, and (Q3) How do the findings from wind tunnel experiments translate to the in-flight performance of an aerial vehicle?

For Q1, our study reveals that a passively deployable covert-inspired flap exploits two location-dependent flow control mechanisms. The first is a previously identified pressure dam
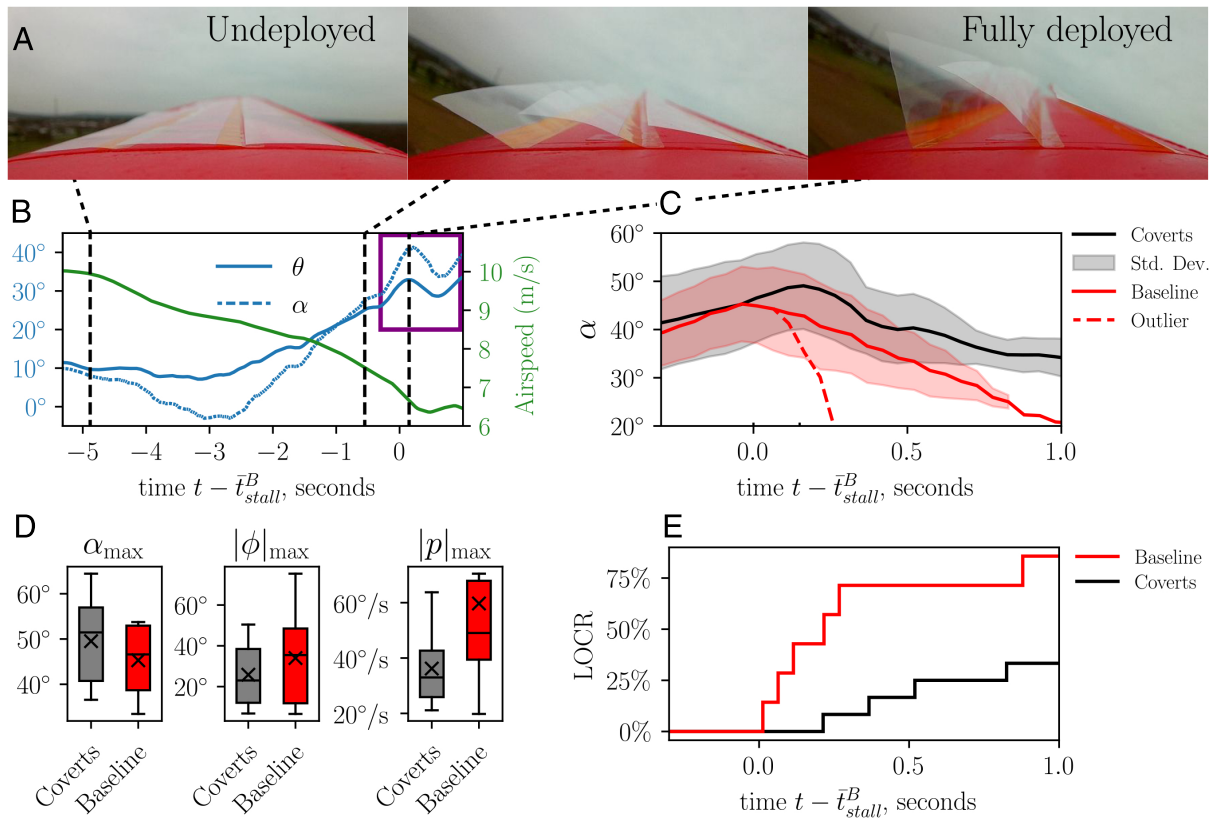
Fig. 5. The effect of covert-inspired flaps on the stall behavior of an autonomous flight demonstrator. Times are offset by the mean baseline stall time $\bar{t}^B_{stall}$. (*A*) Frames showing covert-inspired flap deployment during the stall sequence. (*B*) Effective aircraft angle of attack α, aircraft pitch angle θ, and aircraft airspeed during a representative power-on stall with covert-inspired flaps. The purple box highlights the region studied in Fig. 5*C*. (*C*) Mean and SD of α vs. *t* for all stalls. Each series is offset to align before $\bar{t}^B_{stall}$. (*D*) Box plots comparing the maximum angle of attack α_{max}, maximum roll angle magnitude $|\phi|_{max}$, and maximum roll angle rate magnitude $|p|_{max}$ during the stall trials. (*E*) Loss of control ratio (LOCR) measures the percentage of trials that have lost control within one second of the start of the stall sequence, requiring a recovery sequence.

effect primarily employed by flaps near the trailing edge, while the second is a shear layer interaction mechanism observed for flaps near the leading edge. For the shear layer interaction mechanism, we find that flap deployment reduces the geometric adverse pressure gradient the flow experiences along the airfoil's surface at high angles of attack, reducing the degree of flow separation. In the case of the pressure dam effect, the flap acts as a splitter plate that shields the upstream airfoil surface from the relatively high-pressure wake behind the airfoil. Both of these mechanisms, using a single flap, improve lift and reduce drag at poststall conditions. We also show various ways to identify these distinct flow control mechanisms, namely via the pressure field, the location of the shear layer edge, or by simply observing the flap dynamics. Flaps that engage the pressure dam mechanism exhibit higher amplitude fluctuations (driven by the wake flow dynamics), while flaps that engage the shear layer mechanism exhibit low amplitude fluctuations, as they are driven by a stable shear layer.

Toward answering the second question (Q2), we demonstrate the additive nature of the shear layer interaction mechanism wherein each additional flap deployed interacts with the shear layer emanating from the upstream flap, increasing the deflection of the shear layer further down, enhancing the suction peak experienced by the airfoil at its leading edge. In contrast, the pressure dam effect is not found to be additive; once the pressure zones are separated by one flap, an additional flap separating the low-pressure zone further does not lead to additional aerodynamic gains. Analysis of the flow field not only demonstrates the additive nature of the shear layer interaction

mechanism but also the potential for simultaneous exploitation of both mechanisms. For example, the largest aerodynamic gain is attained when all five flaps along the airfoil suction side are allowed to deploy. Specifically, an airfoil with the all-flap system experiences poststall lift improvements of up to 45%, drag reduction of up to 31%, and enhanced pitch or longitudinal stability. These aerodynamic benefits are also accompanied by noticeably gradual stall properties at angles of attack up to 30°, which is more than 14° beyond the stall angle of attack for the baseline case.

Motivated by the experimental success of covert-inspired flow control in a controlled wind tunnel environment, we implement the multirow covert-inspired flap system on a remote-controlled aircraft, answering the third question (Q3) about the feasibility of applying such a passive and bioinspired flow control system in the field. The flight test shows that the covert-inspired flaps indeed increase the vehicle's performance and expand the flight envelope, increasing the stall angle of attack by 9% and softening the sharp and sudden stall characteristics of the baseline aircraft. These findings from the flight test are in line with the wind tunnel experiments.

The feather-inspired distributed flow control strategy outlined in this article offers a pragmatic approach to expanding the operational capabilities of future aerial vehicles and forms biologically relevant hypotheses about bird flight. For UAVs, the effectiveness, minimal power requirements, and simple implementation of the covert-inspired flaps make them particularly valuable for applications requiring extensive operational ranges

and diverse missions. They may also prove practical in other domains where separation control and mitigation are of great importance, such as the wind energy and automotive industries.

For biology, the results provide a perspective on the aerodynamic function of covert feathers in avian flight. For example, covert feathers in birds are found toward the leading edge of the wing. This study suggests that, upon deployment, the suction side covert feathers may mainly interact with the shear layer rather than forming a pressure dam, as previously suggested. Moreover, the additive nature of the shear layer interaction flow control mechanism, as uncovered in this study, suggests an aerodynamic benefit for having multiple rows of covert feathers, all toward the leading edge of the wing.

The insights about the aerodynamic role of covert feathers should be used to form hypotheses for further testing on birds, given the simplifications adopted in the engineering analogy. The engineered system presented in this work elucidates the fundamental flow physics of covert-inspired flaps by simplifying some of the complexities inherent in the aerodynamics of a bird's wing. For example, while this wind tunnel study employs a two-dimensional wing without twist or chord length variation, bird wings are three-dimensional, exhibiting varying thickness, camber, and twist along their span. Consequently, the stall onset for bird wings is likely less severe than for the two-dimensional airfoil section tested here. Additionally, while the airfoil-flap system mimics the multirow feather distribution found on bird wings, it does not capture the discrete nature of feathers along the span.

The results in this study are enabled by following a bioinspired design process that is rooted in developing biologically relevant yet simplified analogies of natural systems and evaluating them under relevant conditions. Based on the improved and fundamental understanding of the flow control mechanisms employed by spatially distributed covert-inspired flaps, we can now increase the fidelity and complexity of the analogy, allowing for more discoveries for engineered vehicles and forming more refined hypotheses about avian flight.

3. Materials and Methods

3.1. Test Facility and Wing Section Design.
The wind tunnel experiments were carried out in the closed-circuit low-speed wind tunnel at Princeton University. A detailed description of the specification of this wind tunnel is given by Breuer et al. (16). Fig. 1C shows a schematic of the wind tunnel facility and the wing test article. The testing was conducted in the third wind tunnel test section, measuring 1.2 × 1.2 m in cross-section and 1.4 m in length with a turbulence intensity of 0.03% of the free stream velocity. The experiments were carried out at Reynolds number $Re = 200{,}000$ using a NACA2414 model with a chord length $c = 0.12$ m and a span $b = 0.28$ m. The equivalent free stream speed was $U_\infty = 26$ m/s. A Velmex B48 rotary table with a stepper motor was used to change the angle of attack of the wing with a precision of $0.0125°$. An acrylic splitter plate at the wing's tip was used to maintain a two-dimensional flow about the airfoil.

There were five possible positions for flap placement along the airfoil's upper surface, as shown in Fig. 1B, leading to 32 unique wing-flap configurations. A binary naming convention is adopted to distinguish between all configurations presented in the paper, where "1" indicates the presence of a flap and "0" indicates the absence of a flap at the corresponding positions. For example, the baseline airfoil without any flaps is represented as "00000," an airfoil configuration with two flaps at positions $0.20\,c$ and $0.50\,c$ corresponds to "10100," and an airfoil configuration with flaps at all locations indicated in Fig. 1B corresponds to "11111." For all 32 configurations, the length of the flap was fixed at 15% of the airfoil chord ($l_f = 0.15\,c = 18$ mm). The flaps were made of 0.127 mm thick Mylar sheet and mounted to the airfoil surface using acrylic-based clear tape with an equivalent torsional stiffness $k = 5 \times 10^{-3}$

N.m/rad. The flaps' deployment and movements were purely in response to the surrounding fluid and not due to any additional actuation or sensory inputs.

3.2. Flow Field and Force Measurements.
Planar PIV was used to acquire time-resolved measurements of the flow around the wing. The PIV setup utilized a Photonics DMX high-speed Nd:YLF 527 nm dual cavity high-repetition laser with an acquisition rate of 1 kHz. The laser head was situated on *Top* of the wind tunnel test section as shown in Fig. 1C, and the laser beam was redirected toward the area of interest via a series of 90° mirrors. The beam's width and focal length are readjusted just before entering the wind tunnel's test section using a series of adjustable converging and diverging lenses so that the focal point of the sheet lies in the center of the region of interest and the sheet's thickness is under 2 mm. After adjusting the beam, it is fanned out into a laser sheet using a −10 mm cylindrical lens. The laser sheet illuminated neutrally buoyant Di-Ethyl-Hexyl-Sebacat particles with an average diameter of 1 μm. Image pairs were taken using a Photron Nova R5 high-speed CMOS camera with a full resolution of 9 MP. The acquired images were processed using multipass cross-correlation in LaVision's DaVis software. A 64 × 64 px square window was used for the first three passes, followed by a 24 × 24 px adaptive window for the following three passes, with 50% overlap between regions. The final PIV vector spacing is 0.82% of the chord length. 1,000 frames obtained over the duration of 1 s are averaged to obtain the time-averaged flow fields presented in *Results and Discussion*. Additionally, the recordings were postprocessed using Xcitex ProAnalyst Motion Analysis Software to extract the flap angular displacement.

The edge of the shear layer is identified from the time-average velocity measurements as the region with the most negative value of du/dy at every given streamwise (x) location,

$$y(x) = \arg\min_y \left(\frac{du(x,y)}{dy} \right). \quad [1]$$

The time-averaged pressure fields are computed from the statistics of the velocity-field measurements using LaVision's pressure solver. The mean pressure gradient is obtained from Reynolds averaging the momentum equation (17, 18)

$$\nabla \overline{p} = -\rho(\overline{\mathbf{u}} \cdot \nabla)\overline{\mathbf{u}} - \rho\nabla \cdot (\overline{\mathbf{u'u'}}) + \mu\nabla^2\overline{\mathbf{u}}, \quad [2]$$

where $\overline{\mathbf{u'u'}}$ is the Reynolds stress term. The divergence of Eq. 2 is taken to produce the Reynolds averaged pressure Poisson equation (17)

$$\nabla^2 \overline{p} = -\rho\nabla \cdot (\overline{\mathbf{u}} \cdot \nabla)\overline{\mathbf{u}} - \rho\nabla \cdot \nabla \cdot (\overline{\mathbf{u'u'}}) + \mu\nabla \cdot \nabla^2\overline{\mathbf{u}}. \quad [3]$$

The Poisson equation is solved using a Poisson solver subject to two boundary conditions. The first Neumann boundary condition is enforced on the boundary of the flow domain of interest based on Eq. 2. The second Dirichlet boundary condition is enforced on the inviscid boundary side of the domain with incoming flow based on Bernoulli's equation $P_{\text{total}} = P_\infty + \frac{1}{2}\rho U_\infty^2$. The pressure coefficient is obtained by calculating the difference between the local pressure and the free stream pressure, normalized by the dynamic pressure of the flow as shown in Eq. 4.

$$C_p = \frac{p - p_\infty}{\frac{1}{2}\rho U_\infty^2}, \quad [4]$$

Force measurements of the 32 configurations were acquired for angles of attack ranging between 0° and 30° using a six-degree-of-freedom ATI Gamma force/torque transducer sampled at 1 kHz. Three randomized independent trials were conducted for each configuration, based on which the average values and 95% CIs of the forces and torques were calculated. To calculate the 95% CI based on a limited number of trials, a student's t-distribution was used. Based on this distribution, the 95% confidence bounds on the true mean value of some quantity x, $\bar{x}$, based on the sample mean $\bar{x}_{\text{sample}}$ is

$$\bar{x} = \bar{x}_{\text{sample}} \pm \frac{t_{\text{ci}}^{\text{df}}\sigma}{\sqrt{n}}, \quad [5]$$

where $t_{\text{ci}}^{\text{df}} = 4.30$ is the t-score value for a confidence interval ci = 95% and degrees of freedom df = 2, σ is the sample SD, and $n = 3$ is the sample

number. The error bars presented in Figs. 2 *A* and *B* and 3 *C* and *F* represent the bounds of Eq. **5**. The lift *L* and drag *D* forces were calculated based on the measured aerodynamic loads in the wing's body frame F_x, and F_y and the airfoil's angle of attack α:

$$L = F_y \cos(\alpha) - F_x \sin(\alpha), \quad D = F_y \sin(\alpha) + F_x \cos(\alpha). \qquad [6]$$

The coefficient of lift C_l and drag C_d are obtained by dividing the lift and drag forces by the dynamic pressure and the planform area of the wing *S*

$$C_l = \frac{L}{\frac{1}{2}\rho U_\infty^2 S}, \quad C_d = \frac{D}{\frac{1}{2}\rho U_\infty^2 S}. \qquad [7]$$

The pitching moment about the aerodynamic center or the quarter chord M_{AC} is obtained based on the measured moment *M* (positive in the pitch-up direction) and the normal force F_y at the airfoil's midchord

$$M_{AC} = M - \frac{c}{4} F_y. \qquad [8]$$

The pitching moment coefficient about the aerodynamic center C_m is obtained by dividing the pitching moment M_{AC} by the dynamic pressure, the planform area of the wing *S*, and the chord length *c*

$$C_m = \frac{M_{AC}}{\frac{1}{2}\rho U_\infty^2 Sc}. \qquad [9]$$

The force/torque transducer has a range of 0 to 32 N for both the x and y channels, a resolution of 1/160 N, and a maximum uncertainty equal to 0.75% of the full-scale load which is equivalent to a lift coefficient uncertainty $C_l = \pm 0.0175$ or $\pm 1.45\%$ of the full-scale range of measured lift coefficients in this study.

3.3. Aerial Vehicle Flight Testing. To evaluate the performance of the covert flaps in flight, we integrated them onto an uncrewed, relevant-scale, fixed-wing aircraft. We then designed an autonomous stall sequence to assess the aircraft at high angles of attack; autonomy was used to create more consistent and repeatable conditions than manual control. The goal of the experiments was to compare the performance of the vehicles at high angles of attack; in particular, to examine the stall angle of attack α_{max} and the characteristics of the stall break (maximum roll angle magnitude $|\phi|_{max}$, maximum roll angle rate magnitude $|p|_{max}$, and LOCR).

For our aircraft, we chose the Maule M-7 remote-controlled aircraft, a 1:6-scale aircraft designed for slow flight and short takeoff and landing operations. The Maule weighs 1.8 kg and has a 1.5 m wingspan. We equipped the Maule with the Pixhawk 6C Mini flight computer (19), which runs the PX4 Autopilot, a popular open-source autopilot and flight controller. In addition to the included inertial measurement unit, magnetometer, and barometer, we equipped the vehicle with an MS4525DO digital airspeed sensor and an M8N global positioning system receiver. This instrumentation enabled fully autonomous flight operations, as well as automatic and detailed logging of flight variables onboard the Pixhawk for analysis.

The autonomous stall sequence was specified by commanding the following control objectives: decrease airspeed (to below the stall speed) while maintaining the current altitude. This was accomplished using the built-in altitude mode of the PX4 flight controller (20), which seeks to maintain altitude given an airspeed setpoint. To override the PX4's built-in safety features (which keep the aircraft above stall speed), the vehicle's minimum and stall speed parameters FW_AIRSPD_MIN and FW_AIRSPD_STALL were both changed to 0.5 m/s, well-below the actual vehicle's stall speed of around 6.5 m/s.

During the stall sequence, the flight controller slows down while maintaining altitude by increasing pitch while decreasing power. As the aircraft slows through its minimum power speed, the power is increased to achieve even lower speeds and higher angles of attack. [This is known in aviation as flying in the "region of reversed command" (15).] This continues until the critical angle of attack is reached and stall occurs. The sequence ends either when the aircraft departs controlled flight (as indicated by an aggressive, uncommanded pitch down or rolling motion), or (if no loss of control occurs) one second after stall. Once the sequence ends, a manual stall recovery is initiated.

Like the wind tunnel testing, the chordwise length of the flap was 15% of the wing's chord ($l_f = 35.6$ mm). The spanwise length of the flap was only 75% of the wing's span ($l_s = 508$ mm) to avoid the flap's interaction with the wing's tip vortex. The aircraft stalled at an average speed of 6.5 m/s. The dynamic pressures from the flow experienced by the flaps at this speed ($\rho U^2/2$) are an order of magnitude lower than those experienced in the wind tunnel testing. To ensure flap deployment at these lower dynamic pressures, we used a lighter (i.e., thinner, $l_t = 0.05$ mm) Mylar flap along with a 0.025 mm thick Kapton tape with lower torsional stiffness. The flaps are arranged in three rows on top of the wing, as depicted in Figs. 1*D* and 5*A*.

3.3.1. Calculated quantities. The PX4 Autopilot logs hundreds of variables, ranging from battery status at 5 Hz to angular acceleration at 50 Hz. The angle of attack α was not explicitly measured but was calculated from the pitch angle θ and flight path angle γ. The flight path angle at time *t* was calculated as follows:

$$\gamma_t = \arctan\left(\frac{z_t - z_{t-1}}{\sqrt{(x_t - x_{t-1})^2 + (y_t - y_{t-1})^2}}\right),$$

where *x, y, z* are the vehicle positions in a fixed local North East Down frame. From there, angle of attack is calculated as follows: $\alpha_t = \theta_t - \gamma_t$. Since this calculation uses the vehicle trajectory to determine flight path angle, it neglects the effect of wind and gusts on the angle of attack.

During each autonomous stall sequence, if the aircraft departs controlled flight, a manual recovery sequence is initiated. The LOCR plotted in Fig. 5*E* measures the percent of the trials that have effectively "lost control" requiring intervention. It is calculated as follows:

$$\text{LOCR}_t = \frac{\text{trials in recovery mode at time } t}{\text{total number of trials}}.$$

3.3.2. Flight logs. A representative log of one of the Coverts flight tests has been uploaded online through PX4's Flight Review service, and is available at this link: Representative Covert Flight Test. Much of the logged data from the flight test, including the vehicle trajectory and flight controller parameters, can be accessed and reviewed.

Data, Materials, and Software Availability. Data from the wind tunnel force and PIV measurements, as well as the flight test data, are available on Zenodo at DOI: 10.5281/zenodo.13831092 (21). All other data are included in the manuscript and/or supporting information.

1. J. J. Videler, *Avian Flight* (Oxford University Press, 2006), p. 288.
2. A. K. Othman, D. A. Zekry, V. Saro-Cortes, K. J. P. Lee, A. A. Wissa, Aerial and aquatic biological and bioinspired flow control strategies. *Commun. Eng.* **2**, 30 (2023).
3. G. K. Taylor, A. C. Carruthers, T. Y. Hubel, S. M. Walker, "Wing morphing in insects, birds and bats: Mechanism and function" in *Morphing Aerospace Vehicles and Structures*, J. Valasek, Ed. (John Wiley & Sons, Ltd., 2012), pp. 13–40.
4. A. C. Carruthers, A. L. Thomas, G. K. Taylor, Automatic aeroelastic devices in the wings of a steppe eagle *Aquila nipalensis*. *J. Exp. Biol.* **210**, 4136–4149 (2007).
5. L. J. Ordaz, *Experimental Analysis of Unsteady Aerodynamic Covert Feather Behavior* (West Virginia University, 2018).
6. X. Wang, J. A. Clarke, The evolution of avian wing shape and previously unrecognized trends in covert feathering. *Proc. R. Soc. B Biol. Sci.* **282**, 20151935 (2015).

7. L. Wang, M. M. Alam, Y. Zhou, Experimental study of a passive control of airfoil lift using bioinspired feather flap. *Bioinspir. Biomim.* **14**, 066005 (2019).
8. C. Brücker, C. Weidner, Influence of self-adaptive hairy flaps on the stall delay of an airfoil in ramp-up motion. *J. Fluids Struct.* **47**, 31–40 (2014).
9. A. Gardner, S. Opitz, C. Wolf, C. B. Merz, Reduction of dynamic stall using a back-flow flap. *CEAS Aeronaut. J.* **8**, 271–286 (2017).
10. D. O. Izquierdo, F. D. Marques, Experimental analysis of passive bio-inspired covert feathers for stall and post-stall performance enhancement. *Meccanica* **56**, 1–19 (2021).
11. A. K. Othman, N. J. Nair, A. Goza, A. Wissa, Feather-inspired flow control device across flight regimes. *Bioinspir. Biomim.* **18**, 066010 (2023).
12. N. J. Nair, Z. Flynn, A. Goza, Numerical study of multiple bio-inspired torsionally hinged flaps for passive flow control. *Fluids* **7**, 44 (2022).
13. G. Bramesfeld, M. D. Maughmer, Experimental investigation of self-actuating, upper-surface, high-lift-enhancing effectors. *J. Aircr.* **39**, 120–124 (2002).
14. N. J. Nair, A. Goza, Fluid-structure interaction of a bio-inspired passively deployable flap for lift enhancement. *Phys. Rev. Fluids* **7**, 064701 (2022).
15. United States Federal Aviation Administration, *Pilot's Handbook of Aeronautical Knowledge* (United States Department of Transportation, Federal Aviation Administration, 2023). https://www.faa.gov/regulations_policies/handbooks_manuals/aviation/faa-h-8083-25c.pdf. Accessed 22 April 2024.
16. K. Breuer, M. Drela, X. Fan, M. Di Luca, Design and performance of an ultra-compact, low-speed, low turbulence level, wind tunnel for aerodynamic and animal flight experiments. *Exp. Fluids* **63**, 169 (2022).
17. B. Van Oudheusden, PIV-based pressure measurement. *Meas. Sci. Technol.* **24**, 032001 (2013).
18. J. Van der Kindere, A. Laskari, B. Ganapathisubramani, R. De Kat, Pressure from 2D snapshot PIV. *Exp. Fluids* **60**, 1–18 (2019).
19. H. Willee, V. Poon, Holybro Pixhawk 6C Mini. https://docs.px4.io/main/en/flight_controller/pixhawk6c_mini.html. Accessed 22 April 2024.
20. H. Willee, V. Poon, Altitude Mode (Fixed-Wing). https://docs.px4.io/main/en/flight_modes_fw/altitude.html. Accessed 22 April 2024.
21. G. Sedky, N. Simon, A. K. Othman, H. Wiswell, A. Wissa, Dataset: Distributed feather-inspired flow control mitigates stall and expands flight envelope. Zenodo. 10.5281/zenodo.13831092. Deposited 24 September 2024.